Electronic structure of phosphorus and arsenic δ-doped germanium

D. J. Carter,[1,2] O. Warschkow,[3] J. D. Gale,[1,2] G. Scappucci,[4] W. M. Klesse,[4] G. Capellini,[5] A. L. Rohl,[1,2] M. Y. Simmons,[4] D. R. McKenzie,[3] and N. A. Marks[6,2]

[1]*Dept. of Chemistry, Curtin University, GPO Box U1987, Perth WA 6845, Australia*
[2]*Nanochemistry Research Institute, Curtin University, GPO Box U1987, Perth WA 6845, Australia*
[3]*Centre for Quantum Computation and Communication Technology, School of Physics, The University of Sydney, Sydney NSW 2006, Australia*
[4]*Centre for Quantum Computation and Communication Technology, School of Physics, The University of New South Wales, Sydney NSW 2052, Australia*
[5] *Dipartimento di Scienze, Università degli studi Roma Tre, Viale Marconi 446, I-00146 Roma, Italy*
[6]*Discipline of Physics & Astronomy, Curtin University, GPO Box U1987, Perth WA 6845, Australia*

(Dated: October 7, 2013)

Density functional theory in the LDA+U approximation is used to calculate the electronic structure of germanium δ-doped with phosphorus and arsenic. We characterize the principal band minima of the two-dimensional electron gas created by δ-doping and their dependence on the dopant concentration. Populated first at low concentrations is a set of band minima at the perpendicular projection of the bulk conduction band minima at L into the (k_x,k_y) plane. At higher concentrations band minima at Γ and Δ become involved. Valley splittings and effective masses are computed using an explicit-atom approach, taking into account the effects of disorder in the arrangement of dopant atoms in the δ plane.

PACS numbers: 61.72.uf, 71.20.Mq, 71.20.Nr, 71.55.Cn

I. INTRODUCTION

Since its first demonstration in 2009 (Ref. 1), phosphorus in germanium (Ge:P) δ-doping is rapidly emerging as a viable technique to achieve high n-type carrier concentrations in germanium. These concentrations are a key requirement for a variety of applications ranging from source/drain contacts in high mobility nanoscale transistors[2] to CMOS integrated Si-compatible lasers.[3–5] Moreover, the highly confined two-dimensional electron gas (2DEG) resulting from the P donor sheet can be patterned with atomic-scale precision using scanning probe lithography and phosphine (PH_3) gas as dopant source to create planar Ge:P nanodevices, such as atomic-scale wires and tunnel gaps.[6] Further, multiple δ-layers can be vertically stacked in the Ge crystal, preserving their individuality from a structural and electrical point of view,[7–9] and opening the possibility of three-dimensional epitaxial circuits comprising vertically stacked 2DEGs and atomic-scale Ge:P devices. Arsenic δ-layers in germanium have not yet been produced by these lithography techniques, but there is no in-principle reason against their fabrication. Indeed, from an ionic radius perspective, arsenic is a more natural fit for germanium. The deposition chemistry of PH_3 and AsH_3 on Si(001) is reported[10] to share many similarities, and hence it is reasonable to surmise that Ge:P fabrication protocols are transferable to Ge:As nanodevice fabrication.

With experimental progress advancing at a rapid pace, a detailed theoretical understanding of the electronic structure of δ-doped Ge is warranted. Few studies have been performed in this area, with the closest studies concerned with germanium nanofilms[11] and Ge/SiGe quantum wells.[12–14] In addition, Hwang and Das Sarma[15] have recently reported transport properties of δ-doped silicon and germanium calculated using Boltzmann transport theory. In this work we present a detailed density functional theory (DFT) study of (001)-oriented δ-doped Ge at phosphorus and arsenic doping concentrations between 1/12 and 1/2 monolayer. Our results provide insight into aspects of the electronic band structure such as band folding, valley splitting, and effective masses as a function of concentration. We examine the effect of dopant disorder on the electronic structure and quantify the differences between phosphorus and arsenic. Valley splittings and effective masses are key parameters for the design of epitaxial circuits assembled with germanium-based 2DEGs and/or devices with confinement in other dimensions, such as quantum wires, tunnel junctions, or quantum dots.

This paper is organized as follows. The basic computational methodology and its validation against the known band structure of bulk germanium is outlined in Section II. In Section III we systematically work through the various technical challenges of performing DFT calculations on Ge:P/As-δ in order to obtain meaningful physical properties for this system. We discuss in turn: the projection of the bulk band structure into the δ-plane (Section III A), the 2DEG band energies and valley splittings of δ-doped Ge as obtained using an approximate mixed-atom model (Section III B), the folding of bands when larger in-plane unit cells are used (Section III C), which is preparatory to the discussion of explicit-dopant models with ordered (Section III D) and quasi-disordered (Sections III E and III F) arrangements of dopant atoms in the δ-plane.

II. METHODOLOGY

Density functional theory (DFT) calculations on δ-doped germanium are conducted by adapting the general approach previously applied to Si:P by ourselves[16–18] and others[19–21] to the specific requirements of Ge:P and Ge:As. All calculations are performed using the SIESTA software.[22] The electronic wavefunctions are expanded in a basis-set of atom-centered numerical atomic orbitals of double-zeta-plus-polarization (DZP) quality. All basis functions are radially confined such that orbital energies shift by 0.02 Ry (see Ref. 22 for details) and a split-norm ratio of 0.15 is used. The effective potentials due to the nucleus and core electrons are represented using norm-conserving Troullier-Martins pseudopotentials[23] and electron exchange-correlation is treated in the local-density approximation (LDA). An auxiliary basis consisting of a real-space mesh with a kinetic-energy cutoff of 300 Ry is used to represent the electron density. Convergence is assisted by the use of Methfessel-Paxton smearing (Ref. 24; polynomial of order 5, T=298 K) With these settings and a 20×20×20 Monkhorst-Pack[25] **k**-point grid, the germanium bulk lattice constant, a, was calculated to be 5.620 Å, in good agreement with the experimental value of 5.66 Å (Ref. 26). This calculated lattice constant is used in all subsequent calculations. All internal atomic positions were held at bulk values.

To address the problem of a vanishing band gap for bulk germanium within local DFT (e.g. Refs. 27–30) we utilize the LDA+U formalism as described by Dudarev *et al.*[31] in our band structure calculations. A single empirical correction of $\bar{U}-\bar{J}$=2.6 eV is applied to all valence p orbitals. Figure 1 shows the calculated band structure of bulk germanium in a face-centered-cubic (fcc) cell with several energy differences labelled. The calculated band gap (Γ–L_{fcc}) of 0.75 eV matches the experimental value of 0.74 eV (Ref. 32) by construction through the choice of $\bar{U}-\bar{J}$. The band energy differences from Γ–Γ (1.02 eV) and Γ–X (1.20 eV) compare well to experiment[27,32,33] where the corresponding (room-temperature) values are 0.90–1.0 and 1.3 eV, respectively. One subtle discrepancy is that the band minimum at Δ is calculated to be slightly more stable than that at Γ, whereas higher levels of theory appear to predict the reverse.[30,34]

The textbook ellipsoidal shape of the conduction band minimum at L_{fcc} is evident in the low curvature of the band along L_{fcc}–Γ and the much higher curvature in the almost perpendicular L_{fcc}–X_{fcc} direction. Each of the ellipsoidal valleys is oriented with its principal (longitudinal) axis along Γ-L_{fcc}, and is cut in half by a hexagon-shaped boundary plane of the fcc lattice Brillouin zone. Effective masses of the ellipsoidal valleys and several other extrema were computed by fitting parabolic functions to the band structure near the minima. By fitting to parabolic functions, longitudinal and transverse effective masses were computed to be 1.61 and 0.10 m_e, respectively, which compare well to experimental values of 1.64 and 0.08 m_e (Ref. 35).

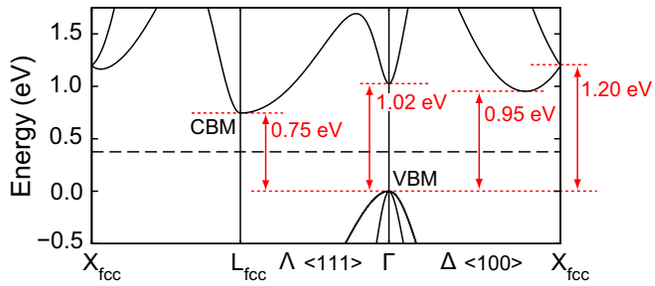

FIG. 1: Calculated band structure of germanium for the 2-atom fcc unit cell using the LDA+U approach as detailed in the text. X_{fcc}, L_{fcc}, and Γ correspond to reciprocal lattice points $(2\pi/a,0,0)$, $(\pi/a,\pi/a,\pi/a)$, and $(0,0,0)$, respectively. The conduction band minimum (CBM) at L_{fcc} and the valence band maximum (VBM) at Γ are indicated together with several band energy differences.

As in our previous work on silicon[17,18] we use two distinct approaches to represent the dopant distribution in the δ layer: *mixed-atom doping* based on the virtual crystal approximation[36,37] and *explicit doping* using discrete distributions of phosphorus, arsenic, and germanium atoms. Explicit doping is the more realistic and hence more accurate representation, however its use is associated with a number of technical complexities that we will address below. In contrast, the approximate mixed-atom approach is intuitive and accessible because a high degree of symmetry is maintained. This is achieved by describing the atoms in the dopant plane as a fractional average between dopant and bulk atoms, which means that *any* dopant concentration can be represented using the smallest possible in-plane repeat. Although δ-doping experiments in germanium have to-date only been performed using phosphorus, arsenic is the more natural choice as noted above. Accordingly, the mixed-atom calculations reported in this work employed hybrid atoms intermediate between Ge and As. We also performed a series of tests using mixed Ge/P hybrid atoms and the band structures were virtually indistguishable from those involving As. Residual quantitative differences are very small indeed, and entirely secondary to the approximations that are intrinsic to the mixed-atom approach.

III. RESULTS

A. Band structure projection into the δ-plane: Bulk

Before we can discuss the effects of doping, we must first understand how the three-dimensional band characteristics of bulk germanium [fcc unit cell; Fig. 1] translate into the two-dimensional band geometry that applies to δ-doping. This requires two sequential lattice transformations: from fcc to primitive tetragonal and from

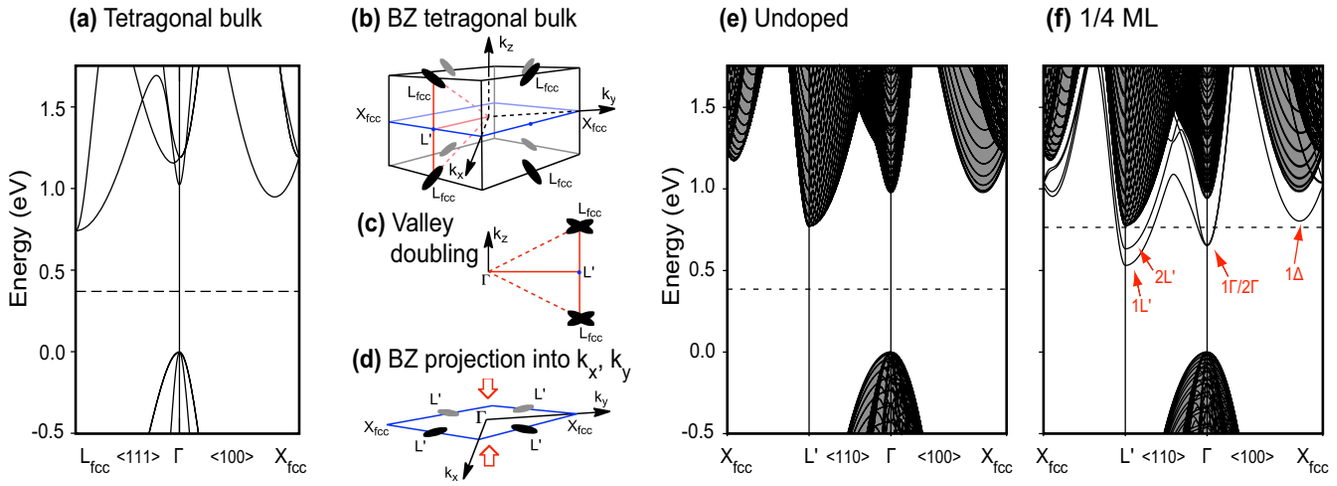

FIG. 2: (a) Band structure of bulk germanium in a four-atom tetragonal unit cell; (b) Schematic view of the Brillouin zone of the tetragonal unit cell and the eight ellipsoidal valleys; (c) Plane view illustrating the intersecting ellipsoidal minima at L_{fcc}; (d) Projection of the L_{fcc}-point conduction band minima into the (k_x,k_y)-plane in an elongated supercell appropriate for δ-doping; (e) Plane-projected band structure for undoped germanium using a 192L supercell with a 1-atom in-plane repeat; (f) Band structure of δ-doped germanium with an arsenic dopant concentration of 1/4 ML computed using a mixed-atom approach and the same supercell as in (e). Calculations used a 16×16×12 **k**-point grid in (a), and a 16×16×1 grid in (e,f). The Fermi level is indicated by dashed lines. For orientation, the projected bulk band structure is shown in (e,f) as a gray-shaded background.

primitive tetragonal to a tetragonal supercell. We discuss these two transformations in turn.

fcc→primitive tetragonal. The orientation of the δ plane in experimental Ge:P-δ-samples is typically (001) and hence we require a unit cell with two lattice vectors within the (001) plane. The smallest bulk unit which satisfies this condition is a four-atom tetragonal unit cell with a 1-atom in-plane repeat. It is instructive to consider first the band structure of bulk germanium in this primitive tetragonal representation which is shown in Fig. 2(a). In comparison to the fcc unit cell (Fig. 1), additional bands arise due to Brillouin zone folding. These additional bands can be understood by considering the tetragonal Brillouin zone shown in Fig. 2(b), and the position and orientation of the ellipsoidal conduction band minima. Note that in this unit cell the L_{fcc} points above and below the k_x,k_y plane become equivalent (being separated by a reciprocal lattice vector in k_z). As illustrated by the plane cut in Fig. 2(c), this causes a pair of ellipsoidal valleys to become co-located at the same point but with their longitudinal axes oriented at an angle of 70.5°. These two orientations are evident in Fig. 2(a) through the appearance of a high-curvature branch around the L_{fcc} band minimum in addition to the low-curvature branch seen in the fcc band structure (Fig. 1).

primitive tetragonal→tetragonal supercell. In order to separate the δ-atomic plane from its periodic image we extend the primitive tetragonal cell along z to create a highly elongated supercell. The corresponding reciprocal lattice is compressed in k_z. In the limit of an infinite supercell, the band structure is completely projected into the (k_x,k_y)-plane. Figure 2(d) illustrates how the conduction band minima at L_{fcc} ($\pm\pi$/a,$\pm\pi$/a,$\pm\pi$/a) project into the (k_x,k_y)-plane to give four doubly degenerate minima at ($\pm\pi$/a,$\pm\pi$/a,0). For convenience, we label these four minima L′. Through geometric considerations it can be seen that each projected minimum is the center of an ellipse with a longitudinal axis that is shortened by a factor of $\sqrt{2/3}$=0.816, whereas the transverse axis remains the same. The situation is more straightforward for the six Δ band minima which are projected as in Si:P δ-doping (see e.g. Ref. 18), i.e. the two out-of-plane minima are projected to Γ and the in-plane minima are left unchanged.

Figure 2(e) displays the band structure of undoped germanium in this elongated unit cell (a 1×1×48 supercell of the tetragonal unit cell implying a repeat of 192 atomic layers in z, which we denote 192L). The folding becomes apparent in two ways; the conduction band minimum at L_{fcc} is mapped to L′=($\pm\pi$/a,$\pm\pi$/a,0) as described above, and a much larger number of bands appear. The gray shading in the background represents the continuum of bands that would arise for a supercell infinitely long in z. This shading is included in some of the subsequent δ-layer band structures as a reference to the bulk continuum. The curvature of this band continuum at L′ demonstrates the elliptical character of the projected conduction band minimum: the steeply curving branch from L′ to X_{fcc} has an effective mass of 0.094 m_e, a near match to the calculated transverse value of 0.10 m_e for bulk germanium. In the L′ to Γ direction the effective mass is 1.073 m_e, precisely two-thirds of the calculated bulk longitudinal value, exactly as expected since the effective mass varies

as the square of the geometric foreshortening.

B. δ-doping in the mixed-atom representation

Having characterized the bulk band structure in the two-dimensional projection, we can now introduce dopant atoms into the δ-plane. We start off here with the more accessible mixed-atom approach to doping. The calculated band structure for a mixed-atom doping concentration of 1/4 ML is shown in Fig. 2(f). The ionized dopant cores in the δ-plane create an attractive potential that pulls several conduction bands into the energy gap. The additional electrons associated with the dopants occupy these bands, which raises the Fermi level from the mid-gap and creates a 2DEG whose electronic properties are determined by these bands. At the L′ point there are two band minima that we label 1L′ and 2L′. The energy difference of 102 meV between these two minima is due to the confining dopant potential, which couples together the two degenerate valleys in the bulk, and causes them to split apart. At the Γ point there are also two band minima, labelled 1Γ and 2Γ which are valley split by a tiny amount (3 meV). Although the 1Δ minima are stabilized by the doping potential, they are not pulled sufficiently far into the gap to be populated.

Similar calculations were performed for mixed-atom doping concentrations of 1/12, 1/8 and 1/2 ML. Quantitative details of the band structures are summarized in Table I. The data shows how the band minima are progressively lowered in energy (i.e. stabilized) with increasing dopant concentration, reflecting the increasing strength of the doping potential. The increase of the L′ valley splitting with doping points to the potential also becoming more confining. Figure 3 further visualizes these trends by plotting the band minima and the Fermi level, E_F, as a function of doping concentration. Interpolated crossings between the band energies and E_F allow us to estimate the concentrations at which successive band minima become occupied. Below 0.1 ML only the L′ minima are lower than the Fermi level and hence this is the only populated region of the band structure. Above 0.1 ML, the bands minima around Γ become involved. A relatively high 0.4 ML are required to populate the band minima at Δ.

TABLE I: Calculated valley splitting, band minima and Fermi level (all in meV) as a function of dopant concentration using the mixed-atom approach and a 192L supercell. Valley splittings (VS) are calculated as the difference between the first two band minima at the L′ and Γ positions. Band minima are expressed relative to the bulk conduction band minimum and are reported at the L′ and Γ points, and along the Δ axis. The same reference is used for the Fermi level.

	1/12 ML	1/8 ML	1/4 ML	1/2 ML
L′	−110	−165	−246	−459
Γ	+29	−41	−124	−310
Δ	+103	+60	+25	−64
VS (L′)	23	42	102	256
VS (Γ)	2	2	3	2
E_F	−4	−9	−13	−29

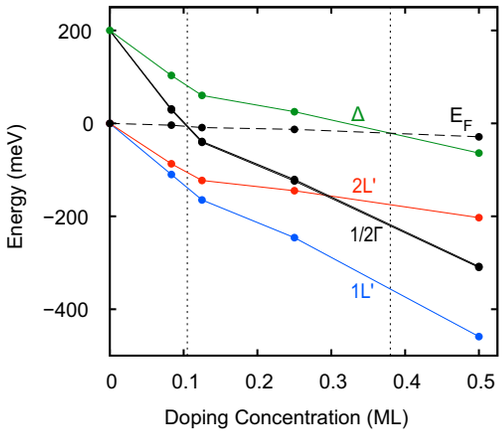

FIG. 3: Band minima and Fermi level as a function of doping concentration using the mixed-atom approach with a 192L supercell. Vertical dashed lines denote the critical dopant concentrations at which successive band minima become populated.

C. Larger in-plane repeats and Brillouin zone folding

Up to this point, our band analysis of δ-doped Ge has relied on the approximate mixed-atom approach to represent the dopants in the δ-plane. This approach is convenient in that it preserves the symmetry of bulk-germanium projected into the (k_x,k_y) planes. The fact that we can represent this system using the smallest possible (i.e. primitive) in-plane repeat unit of one atom is a practical consequence of this symmetry. However, this symmetry no longer applies when we switch to the more accurate explicit-dopant model and the larger in-plane repeats required for this approach. In this section, we describe how the mixed-atom band structures carry over into larger in-plane repeat units. This prepares the ground for the explicit-dopant model discussed in the following sections.

A larger in-plane repeat in real space corresponds to a smaller Brillouin zone in reciprocal space into which a larger number of bands and valleys are folded. Figure 4 shows the 1/4 ML mixed-atom band structure when moving from a 1-atom in-plane repeat [Fig. 4(a)] to a 2-atom repeat [Fig. 4(b)], and from there to an 8-atom repeat [Fig. 4(c)]. Shown with each band structure are schematic sketches that indicate how the L′, Γ and Δ band minima become repositioned as the Brillouin zone shrinks in size.

The 1-atom band structure shown in Fig. 4(a) is es-

sentially the same as that in Fig. 2(f) except that it was obtained using a more compact 80L model. This out-of-plane shortening of the supercell is necessary in order to render the larger in-plane repeats computationally feasible. Valley splittings of 100 and 3 meV at L′ and Γ, respectively, compare favourably with those obtained for the larger 192L model (102 and 3 meV), suggesting that this shortened model is suitable for the purpose of calculating valley splittings. The band structure for the 2-atom repeat [Fig. 4(b)] differs from the 1-atom repeat in two distinct aspects: (i) the 1Δ band is folded closer to the Γ point from $0.80\times2\pi/a$ along <100> to $0.20\times2\pi/a$, and (ii) new high curvature branches appear at the 1L′/2L′ band minima. These new branches are associated with a doubling of the elliptic band valleys at the L′ point due to band folding. As indicated in the Brillouin zone schematic, the pair of valleys are oriented at a 90° angle, such that both the longitudinal and transverse directions appear on the L′-Γ axis as low- and high-curvature branches around L′, respectively. Moving from a 2-atom repeat to an 8-atom repeat [Fig. 4(c)] introduces further band folding associated with a reduction of the Brillouin zone to a quarter in size. In an 8-atom repeat, the valleys at L′ are mapped to the Γ point, while the positions of the Δ minima are unaffected. We note that the same band positions apply to 4- and 16-atoms repeats (not shown here).

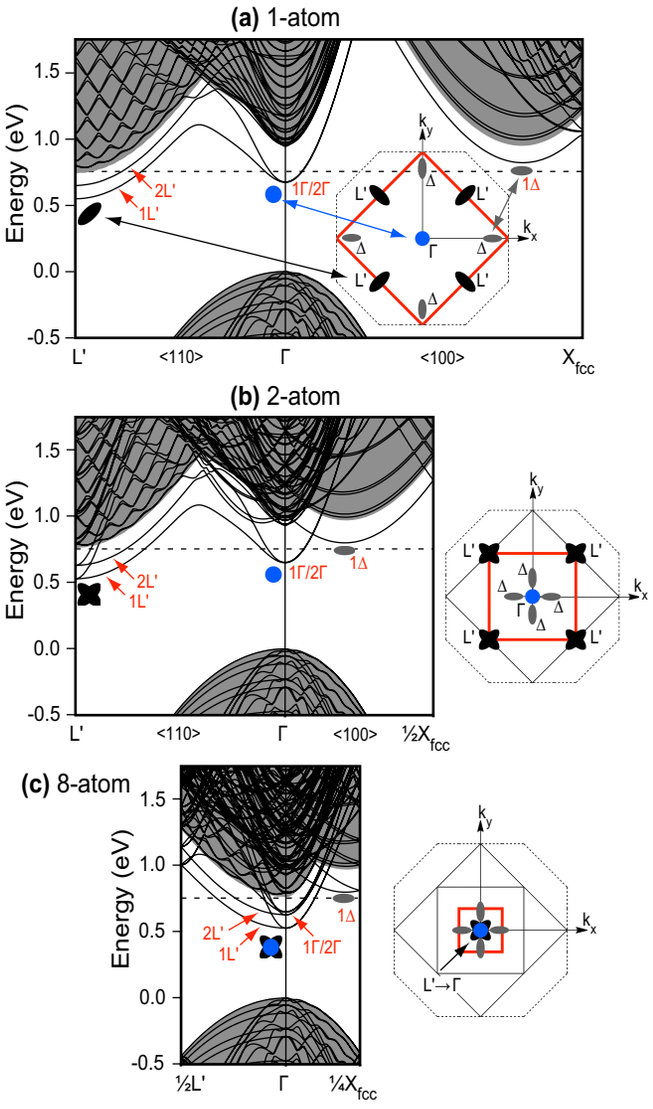

FIG. 4: Illustration of band folding in 1/4 ML δ layers when moving to larger in-plane repeats. (a) Band structure and schematic illustration of the two-dimensional Brillouin zone for a 1-atom repeat unit, with the position of the L′, Γ, and Δ band minima indicated. (b) Same as (a) for a 2-atom repeat. (c) Same as (b) for a 8-atom repeat. All calculations performed using the mixed-atom approach with an 80L supercell.

There are two key points to take away from this analysis: (1) Reciprocal lattice positions that are distinct for a primitive 1-atom repeat can become coincident for a larger repeat. Correspondingly, band valleys that are separate and apart can become overlapping. We saw an example of this earlier [*cf.* Fig. 2(b,c)] when a switch from a fcc bulk cell to primitive tetragonal caused two three-dimensional ellipsoidal valleys to overlap at a 70.5° angle. The same occurs here for δ-doped Ge and in-plane repeats of four atoms and larger; two sets of 1L′/2L′ elliptical valleys oriented at a 90° angle become coincident at the Γ-point, joining the 1Γ/2Γ band minima already there. One of the challenges in the following discussion will be to separate these bands from one another. (2) Band folding *alone* does not cause any coincident bands to interact; this requires an interaction (here: a doping potential) that breaks the symmetry of the primitive cell. The mixed-atom approach preserves symmetry because all atoms in the δ-plane remain equivalent, and hence properties such as band energies and valley splittings are the same, irrespective of the size of the in-plane repeat used. In contrast, the explicit-doping approach will typically be symmetry-breaking. This introduces new interactions and band splittings in addition to those seen in the mixed-atom model. The challenge will be to identify the valley splitting amongst these other interactions.

D. Explicit-dopants: Ordered

In the explicit doping approach, a discrete distribution of germanium, arsenic and phosphorus atoms is used to achieve a more realistic representation of δ-doping in germanium. Explicit doping requires us to not only define the number of dopant atoms in the δ atomic plane, but also their placement relative to one another. The dopant arrangements considered in this section are maximally ordered, in that they are described by a primitive *dopant repeat pattern* that contains only a single dopant atom. This is to say that all dopant atoms are symmetry related to one another by the shortest possible translational repeat vectors. Taking the example of 1/4 ML doping,

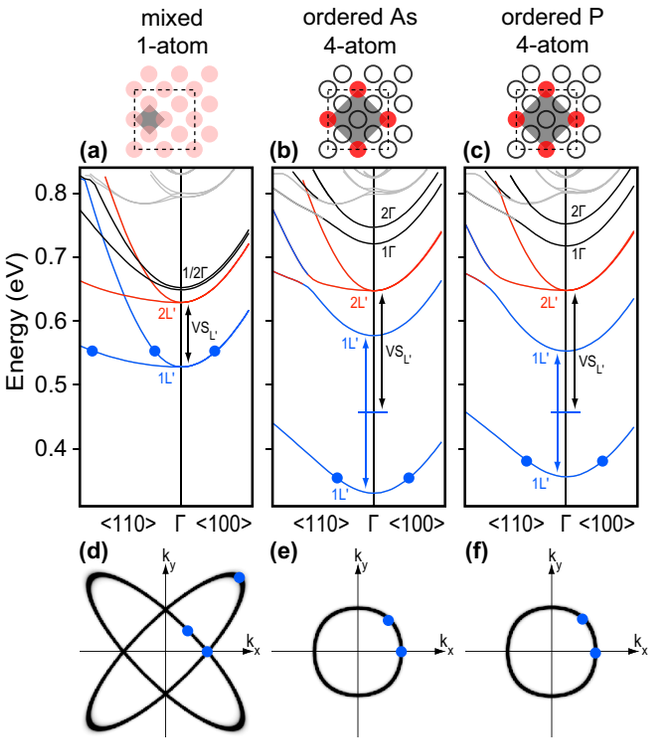

FIG. 5: Band structure near the Γ point showing (a) 1/4 ML mixed-atom doping; (b) 1/4 ML explicit-doping using an ordered 4-atom arsenic dopant repeat pattern; (c) same as (b) but using phosphorus dopants. The 1L′, 2L′ and 1Γ/2Γ bands are colored blue, red and black, respectively. Individual bands change color as they undergo avoided crossings. The bands are plotted one-quarter of the way to the zone boundary in each direction. The light-gray shading in the schematics highlights the dopant repeat unit, while the dashed lines indicate the in-plane repeat unit. (d-f) Transverse cuts in the k_x,k_y plane through the band structure above, showing the valley shape at 25 meV above the lower 1L′ band minimum. Blue circles are used to indicate corresponding points in the band structure. All calculations employ an 80L supercell with a 6×6×1 **k**-point grid.

the maximally ordered dopant arrangement contains four atoms, three Ge and one As or P, in a square-shaped 4-atom repeat pattern.

The calculated band structure for 1/4 ML δ-layer using mixed-atom doping, explicit As doping, and explicit P doping are shown in Fig. 5(a-c). These plots focus on the immediate vicinity of the Γ-point in order to better bring out the folded 1L′/2L′ and Γ band minima. The specific dopant placement pattern used is illustrated by the schematic above the band structure, where we have indicated the primitive dopant repeat pattern (1-atom for mixed, 4-atom ordered for explicit) using background gray shading. Note that the computational supercell used in these calculations has an 8-atom in-plane repeat unit which is indicated by dashed lines in the schematics. This larger unit cell will later facilitate comparisons with other (more disordered) dopant arrangements.

Looking first at the mixed-atom calculation [Fig. 5(a)] we can attribute various L′ and Γ minima by their folding in Fig. 4. For clarity, we have highlighted the 1L′ and 2L′ bands (both low and high curvature branches) using blue and red colored lines, respectively. The 1Γ and 2Γ bands are shown using black lines, and other bands are shaded gray. Shown underneath the mixed band structure is a transverse cut in the k_x,k_y plane [Fig. 5(d)] at an energy of 25 meV above the 1L′ band minimum. This type of diagram neatly brings out the shape of the two degenerate elliptical valleys crossing at an angle of 90° at Γ [*cf.* Fig. 4(c)].

The band structure of the arsenic explicit-ordered case [Fig. 5(b)] is at first glance quite different from that of the mixed case [Fig. 5(a)]. We recognize the 2L′ band (red lines) from the mixed case which is largely preserved in the explicit case with a low and high curvature branch along <110> that is indicative of a degenerate pair of elliptical valleys crossing at an angle. We can also spot the pair of 1Γ/2Γ bands (black lines) by their curvature. These bands are shifted up in energy by about 0.1 eV relative to the mixed-atom case, and the valley splitting is notably increased from 3 to 25 meV. In contrast, the 1L′ bands (blue lines) exhibit hardly any resemblance to the mixed case, having split from a degenerate pair to become two separate bands. Closer inspection shows that the curvature of these bands along <100> is similar to that in the mixed case, and along <110> it is intermediate between that of the high- and low-curvature branch of the mixed case. Collectively, these observations point towards a strong coupling between the pair of 1L′ elliptical valleys that results in their splitting apart. This hypothesis is further supported by the k_x,k_y cut [Fig. 5(e); again at 25 meV above the band minimum]: the valley shape is now very nearly isotropic with only a small amount of bulging along the <110> directions, indicative of an equal-sized combination of the two elliptical valleys.

We will show in the next section that the interaction that couples the two degenerate 1L′ valleys is due to the high degree of order in the dopant arrangement. This interaction is in addition to the genuine valley splitting $VS_{L'}$ that is due to two-dimensional confinement, and hence we need to separate one from the other. This is done here by simple averaging as is indicated by double arrows in Fig. 5(b), i.e. we calculate $VS_{L'}$ as the average difference between the two 1L′ band minima and 2L′.

TABLE II: Valley splittings (VS, in meV) of the L′ and Γ band minima calculated for the 1/4 ML explicit-ordered and mixed-atom representations (*cf.* Fig. 5). Also included are longitudinal and transverse effective masses (in units of m_e) for the 1L′ and 2L′ bands.

	$VS_{L'}$	VS_Γ	$m^*_{1L'}$	$m^*_{2L'}$
1-at. Mixed	100	3	1.09/0.10	0.92/0.10
4-at. Ordered As	193	25	0.20/0.19	0.82/0.10
4-at. Ordered P	193	34	0.21/0.19	0.76/0.10

From this we derive an L′ valley splitting of 193 meV, which is almost twice the value obtained using the mixed-atom approach. As noted previously in the context of Si:P δ-doping[17,18] the mixed-atom approach, for all its intuitive utility, tends to underestimate valley splittings.

Figure 5(c) shows the band structure for the same 1/4 ML explicit-ordered dopant pattern, except that phosphorus is now used as the dopant. Comparison with Fig. 5(b) reveals that the band structures of As and P are in qualitative terms almost identical. The L′ valley splitting remains unchanged at 193 meV. The Γ valley splitting increases from 25 to 34 meV. Selected band structure properties for 1/4 ML mixed-atom doping, and the two explicit-ordered doping models are summarized in Table II. With the explicit-atom approach the curvature of the heavy 1L′ branch is significantly decreased, but as we show below, this difference is a consequence of ordering in the dopant pattern rather than a reflection of the choice of pseudopotential employed. We also see that the effective masses in the two explicit-ordered structures are extremely close, confirming that arsenic and phosphorus exhibit similar behaviour.

E. Explicit dopants: effect of disorder

Experimental evidence does not indicate that dopants are ordered in the δ-plane,[8,9] and hence the maximally-ordered arrangement discussed in the previous section may not be representative of a real sample. In DFT calculations, we can emulate some of the effects of dopant disorder by using repeat patterns that are larger, so that they contain more than just a single dopant atom. Having these additional dopant atoms affords more flexibility to break the high degree of translational symmetry of an ordered pattern. In this section we will specifically focus on a simple 8-atom pattern containing two arsenic or phosphorus atoms to create a minimalist model of 1/4 ML Ge:P/As-δ with dopant disorder.

Band structures for this 8-atom disordered pattern for arsenic and phosphorus are shown in Fig. 6, along with the mixed-atom band structure which is again included for reference. As before, we can match common features such as the band curvature between the mixed and explicit-disordered band structures, and thereby assign individual bands to 1L′ (blue lines), 2L′ (red lines) and 1Γ/2Γ bands (black lines). While the qualitative shape of the individual bands is very similar to their mixed-atom counterparts, the bands are shifted relative to one another. In addition, both 1L′ and 2L′ bands split into two sets, which is most evident in the 1L′ levels. In sharp contrast to the explicit-ordered case discussed earlier [Fig. 5], the 1L′ bands maintain their high and low curvature branches along <110>. This suggests that the strong coupling between the two 1L′ elliptical valleys in the explicit-ordered case does not occur here. That said, the degeneracy of these valleys remains broken.

In order to understand this, we need to look at the 8-

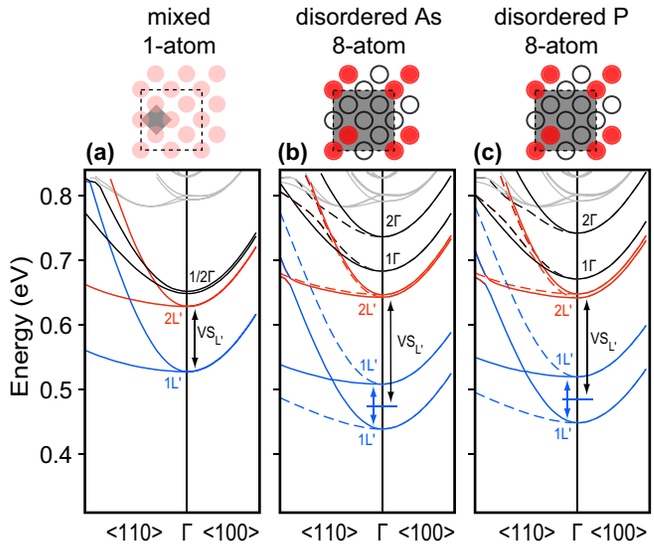

FIG. 6: Band structure near the Γ point using mixed-atom and explicit-doping representations with the in-plane doping pattern indicated by the schematics above each panel. The 1L′, 2L′ and 1Γ/2Γ bands are colored blue, red and black, respectively. Individual bands change color as they undergo avoided crossings. The bands are plotted one-quarter of the way to the zone boundary in each direction. The light-gray shading in the schematics highlights the dopant repeat unit, while the dashed lines indicate the in-plane repeat unit. All calculations employ an 8-atom in-plane repeat, an 80L supercell with a 6×6×1 **k**-point grid.

atom dopant pattern that is shown above the band structures in Fig. 6. The key point to observe here is that the [110] and [$\bar{1}$10] directions are inequivalent in this pattern; a fact that is unavoidable with two dopants and an 8-atom in-plane repeat. This directional inequivalence in turn means that the band structure along the corresponding reciprocal directions will be different. In the Fig. 6 band structures, we have actually plotted the two directions together using solid and dashed lines for [110] and [$\bar{1}$10], respectively, which makes these differences apparent. Keeping in mind that the low-curvature branch corresponds to the longitudinal axis of an elliptical valley, we can see that the lower of the two 1L′ valleys is oriented with its longitudinal axis along [$\bar{1}$10], while the higher valley is oriented along [110]. The broken degeneracy in the 1L′ valleys can thus be attributed to directional inequivalency of the dopant potential. The same occurs for the 2L′ bands, except that the splitting is much smaller and the [110]-oriented valley is the preferred orientation.

The band structures for arsenic [Fig. 6(b)] and phosphorus [Fig. 6(c)] are again very similar. As before, we calculate the confinement valley splitting $VS_{L'}$ as the average energy difference between 1L′ and 2L′. From this we derive L′ valley splittings of 171 and 160 meV for a simple model of 1/4 ML disordered arsenic and phosphorus in δ-doped germanium, respectively. These valley splittings are still considerably larger than the 100 meV

obtained from the approximate mixed-atom approach. However, they are also notably reduced from the explicit-ordered model (193 meV; *cf.* Table II), which highlights the importance of taking dopant-disorder effects into account. Key band structure parameters of this 8-atom explicit-disordered model are summarized in Table III. In contrast to the earlier ordered calculations (see Table II), we see here that the effective masses of the explicit-atom band structures are very similar to the mixed case, and again that arsenic has a similar effect to phosphorus.

F. Disorder without directional inequivalency via a coarse grid approach

In a realistically disordered dopant arrangement, the [110] and [$\bar{1}$10] directions should of course be fully equivalent, and the same applies to the [100] and [010] directions. These constraints are not satisfied by the 8-atom explicit-disordered pattern discussed in the previous section which caused the degenerate L′ valleys to split in energy [*cf.* Figs. 6(b,c)]. In this section we switch to a larger 16-atom repeat, which is the smallest unit that can accommodate 1/4 ML explicit-disordered dopants without introducing directional inequivalencies. The specific phosphorus dopant arrangement patterns considered here are shown in Fig. 7 together with their associated band structures. We compare the 8-atom repeat pattern of the previous section with two types of a 16-atom pattern. All three patterns are equivalent in [100] and [010]; however, only the two 16-atom patterns are also equivalent in [110] and [$\bar{1}$10].

The larger unit cell used in these calculations (16-atoms by 80L, or 1280 atoms in total) is computationally taxing, requiring a truncation of the model in some other aspect to remain feasible. This was achieved here by switching to a coarse sampling of the Brillouin zone using a **k**-point mesh that is about half as dense as used elsewhere in this work.[39] Comparing the 8-atom explicit-disordered pattern [Fig. 7(a)] obtained using the coarse approach with its full model counterpart [Fig. 6(c)], we see that the qualitative characteristics of the band structure are almost entirely preserved. This includes the significant splitting of the 1L′ bands due to directional inequivalence, and the much smaller splitting of the 2L′ bands. Quantitative differences occur in the band energies, which are upshifted by approximately 50 meV, and the valley splittings, which are reduced by approximately 15 meV. For the purpose of assessing the effects of explicit disorder without any directional artefacts, these differences are acceptable.

TABLE III: Calculated valley splittings (VS, given in meV) of the L′ and Γ band minima for the 8-atom disordered dopant distributions shown in Figs. 6. Also shown are the averaged longitudinal and transverse effective masses (in units of m_e) for the 1L′ and 2L′ bands.

	$VS_{L'}$	VS_{Γ}	$m^*_{1L'}$	$m^*_{2L'}$
1-at. Mixed	100	3	1.09/0.10	0.92/0.10
8-at. Explicit As	171	53	0.85/0.11	0.89/0.10
8-at. Explicit P	160	70	0.87/0.11	0.90/0.10

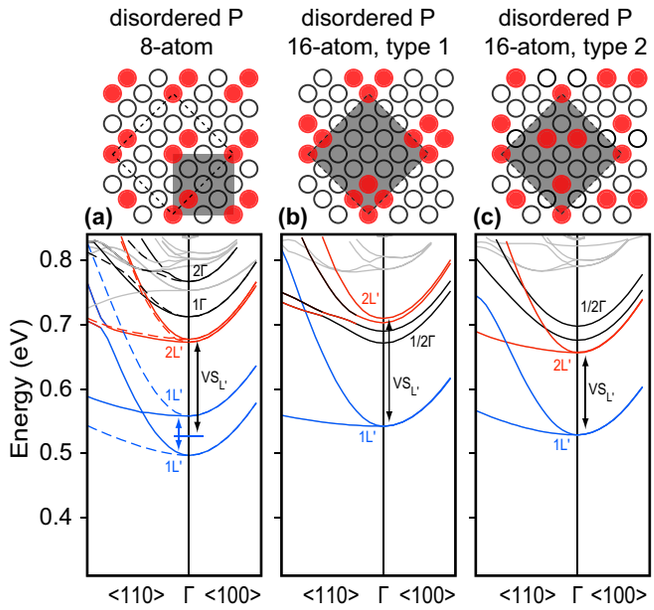

FIG. 7: Band structure near the Γ point using explicit phosphorus dopants and the coarse **k**-point model.[39] Shown are band structures for (a) an 8-atom disordered dopant repeat pattern and (b,c) two types of a 16-atom disordered repeat pattern. The dopant in-plane repeat is indicated using gray background shading. 1L′, 2L′, and 1Γ/2Γ are colored blue, red, and black, respectively. All calculations were conducted using an 80L supercell with a 16-atom in-plane unit cell which is outlined in the schematic using dashed lines.

Looking now at the band structures of the 16-atom explicit-disordered models [Figs. 7(b,c)], it is immediately evident that the L′ valleys are again degenerate. Only a single minimum is seen for the 1L′ band (blue lines) with a low and a high curvature branch along <110>, which indicates a pair of elliptical valleys crossing at a 90° angle. The 2L′ valleys (red lines) are also degenerate for the type 2 pattern [Fig. 7(c)], whereas a small amount of splitting occurs for the type 1 pattern [Fig. 7(b)], presumably due to the 2L′ bands being closely entangled with the 1Γ/2Γ bands. Overall, the qualitative similarities between the 16-atom explicit-disordered band structures to those of the mixed-atom approach [e.g. Fig. 5(a)] are striking. Common to all is that the L′ band minima undergo valley splitting into two sets, namely 1L′ and 2L′. Each is composed of a degenerate, or almost degenerate, pair of 90° rotated valleys due to the Brillouin zone folding as discussed in Section III C. The strong coupling of these valleys seen in the ordered cases [*cf.* Fig. 5(b,c)] is absent, as is the breaking of degeneracy due to the directional inequivalency of the 8-

TABLE IV: Calculated valley splittings (VS, given in meV) of the L′ and Γ band minima for the disordered dopant distributions shown in Fig. 7. These results were obtained using the coarse **k**-point model.[39] Also reported are longitudinal and transverse effective masses (in units of m_e) for the 1L′ and 2L′ bands. Where 1L′ and 2L′ are split, averaged effective masses are reported. For reference, the mixed-atom results (full model) are also included.

	$VS_{L'}$	VS_Γ	$m^*_{1L'}$	$m^*_{2L'}$
1-at. Mixed	100	3	1.09/0.10	0.92/0.10
8-at. Explicit P	147	55	0.86/0.11	0.82/0.10
16-at. Explicit P (type 1)	164	18	1.98/0.11	0.21/0.25
16-at. Explicit P (type 2)	127	22	0.85/0.11	0.80/0.10

atom dopant arrangement [*cf.* Fig. 6(b,c)].

Valley splittings and effective masses for all of the coarse-model dopant patterns in Fig. 7 are listed in Table IV. For reference, data for the mixed-atom representation using the full model is also shown. There are several important points to note. Firstly, the effective masses for the 8-atom explicit-disordered pattern are very similar to those of the corresponding full model listed in Table III. Secondly, the substantial differences in effective masses between the two 16-atom patterns shows that the dopant placement has a strong effect on the curvature of the bands. Our assessment is that the type 2 pattern provides a superior representation of dopant disorder as it avoids the strong interactions which are apparent for the type 1 pattern. The final point is that the effective masses of the 16-atom type 2 pattern are virtually the same as those of the 8-atom explicit-disordered pattern. From this we learn that an 8-atom in-plane repeat is sufficient to compute effective masses, even though the band structure exhibits strong directional inequivalence.

IV. DISCUSSION & CONCLUSIONS

Using density functional theory in combination with mixed-atom and explicit-atom approaches we have quantified the electronic structure of δ-doped germanium. The mixed-atom approach allows the identification of the three primary band minima of the two dimensional electron gas (2DEG) and their variation with dopant concentration. The band structure of the 2DEG is characterized by a set of minima at $(k_x,k_y)=(\pm\pi/a,\pm\pi/a)$, that is, the plane perpendicular projection of the bulk conduction band minima into the plane. For concentrations up to 0.1 ML these are the only occupied bands, while at higher dopant concentrations bands centered at Γ are occupied. Only above concentrations of around 0.4 ML are the Δ minima near $(\pm1.6\pi/a,0)$ and $(0,\pm1.6\pi/a)$ occupied. This behavior contrasts with that of silicon where the first bands of the 2DEG to be populated are centered at the Γ minimum and only two sets of band minima are pulled into the band gap by the doping potential. Another important difference is that the Bohr radius of a donor in germanium is around 80 Å, as compared to around 30 Å in silicon.[40] Consequently, the plane-perpendicular extent of a 2DEG in germanium is larger than in silicon. One practical implication of this difference is that substantially larger unit cells are required to isolate the δ-layers from their periodic images. Specifically, when we performed 40L calculations in germanium the δ layer was clearly not isolated, whereas in previous silicon work 40L was sufficient.[17,18,20]

The explicit-atom approaches are complementary to the mixed-atom calculations and highlight the difficulties faced when describing a disordered two-dimensional layer of explicit-atom dopants. The first problem is computational, since much larger in-plane repeat units are required which constrains the doping concentrations that can be explored. This in turn complicates interpretation of the bandstructure as most of the relevant band minima are folded to the Γ point. A second problem is that the smallest possible representation for a given dopant concentration is artificially ordered due to periodicity, and this ordering introduces a large and unphysical splitting of the principal band minima. To represent disorder with explicit atoms even larger cells are required, in which an additional consideration is the relative placement of the dopants. If the dopant pattern is anisotropic with respect to the underlying band structure then additional bands arise due to orientational splitting between the elliptically-shaped conduction band minima. Accordingly, a 16-atom in-plane repeat is the smallest possible system which can exhibit a degree of disorder and not be anisotropic. Systems of this size are computationally very demanding and require a substantially coarser sampling of the Brillouin zone to be practical.

In addition to the largely qualititative understanding discussed above, the simulations quantify several important transport-related details of the band structure, in particular the valley splitting and effective masses. These quantities are an important input to device-scale modelling such as employed in Ref. 41. The exact value of the L′ valley splitting is dependent on the particular model employed, spanning a range of 100 to 193 meV. The largest splittings occur for highly ordered dopant patterns which are unrealistic and unlikely to be achievable experimentally, while the lower value was obtained using the mixed-atom model which describes the dopant plane using hybrid atoms. Our best estimate for a 1/4 ML Ge:P doping concentration is that the valley splitting is in the vicinity of 140 to 160 meV, with the latter value coming from Table III and the former from Table IV, noting that the splitting in a coarse model of an 8-atom dopant pattern was 13 eV smaller than the corresponding full model.

Effective masses are less dependent on the model employed, with even the mixed-atom approach providing similar estimates to many of the explicit-atom models. The only models to exhibit significant variability are the

unrealistic highly ordered arrangements in Table II and the clustered type 1 arrangement in Table IV. The light effective masses are virtually identical to the bulk value at the L point, while the heavy effective masses are to first order explained by a simple geometric projection of the ellipsoidal valleys into the k_x,k_y plane. The main difference to note is that the 1L′ heavy branch has an effective mass around 20% smaller than the mixed-atom models, with a smaller difference seen for 2L′. Finally, we note that the band strutures of arsenic and phosphorus δ-layers have many common features, with valley splittings and effective masses being very similar. In the case of valley splittings, the differences are typically no more than 10-15 meV. Although Ge:As δ-layers have not yet been fabricated, there is no *a priori* reason against doing so, and the calculations suggest that they too would be promising candidates for 2DEG's in nanoscale devices.

Acknowledgements

This work was supported by the Australian Research Council (ARC) through the Centre of Excellence for Quantum Computation and Communication Technology (Project No. CE1100096). The project used computational resources provided by the iVEC facility at Murdoch University. G.S. acknowledges support from the ARC (Project. No. DP130100403). JDG, NAM and MYS also thank the ARC for fellowships.

[1] G. Scappucci, G. Capellini, W. C. T. Lee, and M. Y. Simmons, Appl. Phys. Lett. **94** (16) (2009).
[2] R. Pillarisetty, Nature **479**, 324 (2011).
[3] D. Liang and J. E. Bowers, Nat. Photonics **4**, 511 (2010).
[4] B. Dutt, D. Sukhdeo, D. Nam, B. Vulovic, Z. Yuan, and K. Saraswat, IEEE Photonics Journal **4**, 2002 (2012)
[5] R. E. Camacho-Aguilera, Y. Cai, N. Patel, J. T. Bessette, M. Romagnoli, L. C. Kimerling, and J. Michel, Opt. Express **20**, 11316 (2012).
[6] G. Scappucci, G. Capellini, B. Johnston, W. M. Klesse, J. A. Miwa, and M. Y. Simmons, Nano Lett. **11**, 2272 (2011).
[7] G. Scappucci, G. Capellini, W. M. Klesse, and M. Y. Simmons, Nanotechnology **22**, 145604 (2011).
[8] G. Scappucci, W. M. Klesse, A. R. Hamilton, G. Capellini, D. L. Jaeger, M. R. Bischof, R. F. Reidy, B. P. Gorman, and M. Y. Simmons, Nano Lett. **12**, 4953 (2012).
[9] G. Scappucci, G. Capellini, W. M. Klesse, and M.Y. Simmons, Nanoscale **5** 2600 (2013).
[10] T. L. McDonell, N. A. Marks, O. Warschkow, H. F. Wilson, P. V. Smith, and M. W. Radny, Phys. Rev. B **72**, 193307 (2005).
[11] A. N. Kholod, A. Saúl, J. D. Fuhr, V. E. Borisenko, and F. A. d'Avitaya, Phys. Rev. B **62**, 12949 (2000).
[12] M. El Kurdi, G. Fishman, S. Sauvage, and P. Boucaud, J. Appl. Phys. **107**, 013710 (2010).
[13] M. Virgilio and G. Grosso, Phys. Rev. B **79**, 165310 (2009).
[14] M. Bonfanti, E. Grilli, M. Guzzi, M. Virgilio, G. Grosso, D. Chrastina, G. Isella, H. von Känel, and A. Neels, Phys. Rev. B **78**, 041407R (2008).
[15] E. H. Hwang, S. Das Sarma, Phys. Rev. B **87**, 125411 (2013).
[16] D. J. Carter, O. Warschkow, N. A. Marks, and D. R. McKenzie, Phys. Rev. B **79**, 033204 (2009); *ibid.* **80**, 049901 (2009).
[17] D. J. Carter, O. Warschkow, N. A. Marks, and D. R. McKenzie, Nanotechnol. **22**, 065701 (2011).
[18] D. J. Carter, O. Warschkow, N. A. Marks, and D. R. McKenzie, Phys. Rev. B **87**, 045204 (2013).
[19] A. Budi, D. W. Drumm, M. C. Per, A. Tregonning, S. P. Russo, and L. C. L Hollenberg, Phys. Rev. B **86**, 165123 (2012).
[20] D. W. Drumm, A. Budi, M. C. Per, S. P. Russo, and L. C. L Hollenberg, Nano. Res. Lett. **8**, 111 (2013).
[21] D. W. Drumm, J.S. Smith, M. C. Per, A. Budi, L.C.L. Hollenberg, and S. P. Russo, Phys. Rev. Lett. **110**, 126802 (2013).
[22] J. M. Soler, E. Artacho, J. D. Gale, A. Garcia, J. Junquera, P. Ordejon, and D. Sanchez-Portal, J. Phys. Condens. Matter **14**, 2745 (2002).
[23] N. Troullier and J.L. Martins, Phys. Rev. B **43**, 1993 (1991).
[24] M. Methfessel and A. T. Paxton, Phys. Rev. B **40**, 3616 (1989)
[25] H. J. Monkhorst, and J. D. Pack, Phys. Rev. B **13**, 5188 (1976).
[26] W. Martienssen and H. Warlimont (Eds.), *Springer Handbook of Condensed Matter and Materials Data*, Springer, Berlin (2005).
[27] W. G. Aulbur, L. Jönsson, and J. W. Wilkins, Solid State Phys. **54**, 1 (1999).
[28] J. Coutinho, S. Öberg, V. J. B. Torres, M. Barroso, R. Jones, and P. R. Briddon, Phys. Rev. B **73**, 235213 (2006).
[29] C. Claeys and E. Simoen, *Germanium-based technologies: From Materials to Devices*, Elsevier BV, Oxford (2007).
[30] P. V. Smith, M. Hermanowicz, G. A. Shah, and M. W. Radny, Comput. Mater. Sci. **54**, 37 (2012).
[31] S. L. Dudarev, G. A. Botton, S. Y. Savrasov, C. J. Humphreys, and A. P. Sutton, Phys. Rev. B **57**, 1505 (1998).
[32] S. Zwerdling, B. Lax, L. M. Roth, and K. J. Button, Phys. Rev. **114**, 80 (1959).
[33] K-H. Hellwege, and O. Madelung (Eds.), Numerical Data and Functional Relationships in Science and Technology, Landolt-Börnstein New Series, Group III, vols. 17a and 22a, Springer, Berlin, (1982).
[34] H. Tahini, A. Chroneos, R.W. Grimes, U. Schwingenschlögl, and H.Bracht, Appl. Phys. Lett. **99**, 072112 (2011).
[35] S. M. Sze, and K. K. Ng *Physics of semiconductors devices*, 3rd Edition, John Wiley & Sons, Inc., New Jersey (2007).
[36] L. Nordheim, Ann. Phys. (Leipzig) **9**, 607 (1931).
[37] L. Bellaiche and D. Vanderbilt, Phys. Rev. B **61**, 7877 (2000).
[38] G. Qian, Y.-C. Chang, and J.R. Tucker, Phys. Rev. B **71**, 045309 (2005).
[39] The 16-atom unit cell is sampled using a 2×2×1 **k**-point

grid. This is slightly less than half the density used elsewhere in this work. The equivalent **k**-point density in an 8-atom unit cell is $2\sqrt{2}\times2\sqrt{2}\times1 \approx 2.8\times2.8\times1$ whereas $6\times6\times1$ is used in our full model.

[40] C. Kittel, *Introduction to Solid State Physics,* 8th Ed., John Wiley & Sons, New York, p. 211 (2005).

[41] M. Fuechsle, S. Mahapatra, F. A. Zwanenburg, M. Friesen, M. A. Eriksson, and M. Y. Simmons, Nat. Nanotechnol. **5**, 502 (2010).